

Global gyrokinetic simulation with kinetic electron for collisionless damping of zonal flow in stellarators

Javier H. Nicolau^{1,*}, Gyungjin Choi¹, Jingyuan Fu², Pengfei Liu¹, Xishuo Wei¹ and Zhihong Lin¹

¹ Department of Physics and Astronomy, University of California, Irvine, CA 92697, United States of America

² Fusion Simulation Center, Peking University, Beijing 100871, People's Republic of China

E-mail: javier.hn@uci.edu and zhihongl@uci.edu

Received 17 June 2021, revised 7 October 2021

Accepted for publication 21 October 2021

Published 12 November 2021



CrossMark

Abstract

Global gyrokinetic simulations with kinetic electrons for collisionless damping of zonal flows in LHD and W7-X stellarators show that the helical components of the equilibrium magnetic field responsible for helically trapped particles have significant impacts on zonal flow. Kinetic electrons reduce zonal flow residue and increase the frequency of low frequency oscillation (LFO). The LFO is induced by dominant helical harmonics of magnetic field strength. Furthermore, linear toroidal coupling of multiple toroidal n -harmonics barely affects the zonal flows, but can generate long wavelength toroidal harmonics with the same toroidal number as the helical magnetic field.

Keywords: simulation, kinetic electrons, stellarator, zonal flow, gyrokinetic

(Some figures may appear in colour only in the online journal)

1. Introduction

The reduction of neoclassical transport in the W7-X stellarator thanks to its quasi-isodynamic design [1] and the finding of an optimized operation regime in the LHD stellarator [2] have shifted research interest from neoclassical to turbulent transport. Recent experiments in the W7-X have shown that a significant amount of transport may be driven by microturbulence [3–5]. The role of spontaneously generated zonal flows in regulating the microturbulence has been extensively studied in axisymmetric tokamaks [6–8]. Zonal flows have also been shown to regulate ion temperature gradient (ITG) turbulence in the LHD and W7-X stellarators in recent global simulations [9]. Therefore, it is important to understand the dynamics of zonal flow and its impact on the microturbulence in the stellarators.

In the past decades, the advances of both analytical theory and gyrokinetic simulations have provided insights of the

dynamics of the zonal flows, which are subjected to collisionless damping by transit time magnetic pumping effects in tokamaks. Rosenbluth–Hinton [10] showed that an initial zonal density perturbation is not fully damped, which results in a residual level due to the neoclassical polarization mostly contributed by toroidally-trapped ions. Xiao–Catto and Wang–Hahm extended the Rosenbluth–Hinton calculations by including shaping effects [11] and dependence on zonal flow radial wavelength [12, 13]. Sugama–Watanabe showed that a residue can survive in the optimized helical configurations with reduced neoclassical transport [14, 15]. A low frequency oscillation (LFO) of the zonal flows was found to be induced by the radial drift of helically trapped particles [16, 17] in the stellarators. The LFO frequency is much smaller than the geodesic acoustic mode (GAM) [18] and has been experimentally observed in the TJ-II stellarator [19].

After earlier work by flux-tube GKV [14] simulations of a simplified LHD-like equilibrium, gyrokinetic simulations of collisionless damping of zonal flows in stellarators have been extended to more realistic equilibrium: LHD [17, 20, 21],

* Author to whom any correspondence should be addressed.

W7-X [17] and TJ-II [22] using global EUTERPE and GT5D codes and flux-tube GENE and GKV codes. Kinetic electrons were found to have little effects on the zonal flow residual level in the tokamaks from the global GTC simulations [23] but can reduce the residual level in the stellarators from the CAS3D-K calculations and GENE and GKV simulations [21, 24].

Despite this progress, important physics of the zonal flow dynamics in the stellarators has not been well studied. First, zonal flows in the stellarators can linearly couple with other toroidal harmonics with $n \neq 0$, unlike in the axisymmetric tokamaks. What are the effects of this linear toroidal coupling on the dynamics of zonal flow and other toroidal harmonics? Secondly, the number of helically-trapped particles could be much more than that of toroidally-trapped particles in some stellarators such as the W7-X. What are the effects of these helically-trapped particles on the zonal flow dynamics? Global simulation is needed to study these unexplored physics since helically-trapped particles may reside in different magnetic field lines and may drift far away across magnetic surfaces. While the effects of a helical magnetic field on the zonal flow damping have been analyzed theoretically in references [14–17], by some simulations with adiabatic electrons [17, 20, 22, 25–31] and by flux-tube simulations with kinetic electrons [21, 24], the impact of (helically-trapped) kinetic electrons is not yet fully understood.

Most of the previous gyrokinetic simulations of microturbulence in stellarators have been local flux-tube simulations which have provided useful insights of turbulent transport. However, the flux-tube simulation [32] makes the usual assumptions of the ballooning mode representation including an axisymmetric equilibrium (i.e. every field line is equivalent), a radially translational symmetry (i.e. high- n ballooning mode approximation), and a finite magnetic shear (i.e. out-going boundary condition along the magnetic field line) [33]. These assumptions are, in general, not valid in the 3D geometry of the stellarators. In fact, recent local and global simulations with adiabatic electrons of zonal flow damping in the HSX and NCSX quasi-symmetric stellarators [30] and the W7-X and LHD optimized stellarators [31] confirm that different flux-tubes produce different zonal flow dynamics in general, and that only some aspects of the zonal flow dynamics in a specific geometry can be recovered from some flux-tube simulations using adequately long parallel flux-tubes. Recently, global gyrokinetic simulations of microturbulence using adiabatic electrons in stellarators have been performed by the EUTERPE [34], GTC [9], XGC-S [35] and GENE-3D [36]. Global simulations are necessary to include the effects of the 3D magnetic field such as the secular radial drift of helically-trapped particles, radial turbulence spreading, linear toroidal coupling of multiple- n toroidal harmonics (i.e. localization of eigenmodes to discrete magnetic field lines), and the linear toroidal coupling between zonal flows and low- n harmonics [9].

In this paper, we study the collisionless damping of zonal flows in the LHD and W7-X stellarators using the global GTC simulations with kinetic electrons. Simulation results show that the helical components of the magnetic field responsible for helically-trapped particles reduce the residue level [24] and

that kinetic electrons increase the LFO frequency. The LFO is induced by the dominant helical harmonics of the equilibrium magnetic field strength. Furthermore, linear toroidal coupling barely affects the zonal flows, but can generate low- n toroidal harmonics with the same toroidal number as the dominant helical component of the equilibrium magnetic field.

The rest of the paper is organized as follows. In section 2 global GTC simulation models for the stellarators are described. Simulation results of collisionless damping of zonal flow are presented in section 3 for the LHD stellarator and in section 4 for the W7-X stellarator. Finally, conclusions are given in section 5.

2. Implementation of the global gyrokinetic simulation model

2.1. Implementation of the model

The numerical simulations presented in this paper are performed using the GTC [6], which is well-benchmarked and extensively utilized for simulations of microturbulence, Alfvén eigenmodes, MHD instabilities and neoclassical transport. The code has recently been upgraded for simulations of Alfvén instabilities in the LHD [37], microturbulence in the W7-X and LHD [9], neoclassical and turbulent transport in the W7-X [38], microturbulence in the DIII-D tokamak with 3D resonant magnetic perturbations [39] and effects of magnetic islands on neoclassical bootstrap current [40] and microturbulence [41]. GTC has also been used to simulate collisionless and collisional damping of the zonal flows in the axisymmetric tokamak and their effects on the turbulent transport [6, 42, 43].

The main goal of this work is to show the effect of kinetic electrons in the zonal flow damping. First, we will perform simulations with ‘adiabatic’ electrons, that is, the electron response is assumed to be zero to the zonal (flux-surface averaged) component of the electrostatic potential, but adiabatic to the non-zonal components. Then the results will be compared with simulations with kinetic electrons solving the drift kinetic equation [44], where the electron response to the zonal component may not be negligible due to helically-trapped electrons. The gyrokinetic model is described in section 2.2.

One important feature of the GTC is that the turbulence mesh used for representing all turbulence quantities (e.g. perturbed density, electrostatic potential, etc) is a global field-aligned mesh in the real space coordinates [45, 46], which achieves the maximal numerical efficiency without making the usual approximation in the ballooning mode coordinates. This turbulence mesh only needs a small number of parallel grid points to resolve drift-wave eigenmode structures, which are elongated in the parallel direction.

The equilibria of the LHD and W7-X, taken from references [9, 47], are calculated by the ideal MHD equilibrium code VMEC [48]. VMEC equilibrium data (magnetic field, metric tensor, etc) are provided by a Fourier series in poloidal and toroidal direction on a discrete radial mesh. The equilibrium data are then transformed to the Boozer coordinates as a Fourier series in the toroidal direction on a discrete 2D mesh

on the poloidal plane. Finally, GTC uses a 3D quadratic spline function defined on an equilibrium mesh to represent these equilibrium quantities for better computational efficiency. Due to the toroidal variations of equilibrium quantities in the stellarator, the number of toroidal grid points in the equilibrium mesh is typically larger than that of the parallel grid points in the turbulence mesh.

When simulating the collisionless damping of the zonal flow in this work, equilibrium density and temperature profiles for both ions and electrons are assumed to be uniform with $T_e = T_i$ to avoid complications of pressure gradients. Simulations are performed in a narrow radial domain so the rotational transform and aspect ratio have little variations within the simulation domain. An initial ion gyrocenter density perturbation is imposed as a sinusoidal function with only radial variations. Zonal flows with various radial wavenumber k_r are simulated. To avoid undesirable effects from the radial boundaries, the perturbation amplitude is enclosed within a Gaussian function so the perturbation is maximum in the center of the radial domain and weak near the boundaries. We analyze the temporal evolution and relaxation of the zonal flows in the simulations. In particular we focus on the zonal electrostatic potential $\langle \phi \rangle$ where the brackets indicate a flux-surface average. In all the simulations presented in this paper, time is given in units of R_0/c_s where R_0 is the major radius, $c_s = \sqrt{T_e/m_i}$, and m_i the ion mass. In the LHD, the magnetic axis is always located in the same location in the poloidal plane for any toroidal angle so R_0 is a constant. However, in the W7-X the location of the magnetic axis varies along the toroidal direction so we take an ‘averaged’ R_0 .

2.2. Gyrokinetic simulation model

We perform GTC linear electrostatic simulations to study collisionless damping of zonal flows in the stellarators. Ion dynamics is described by the collisionless gyrokinetic equation [49, 50]

$$\frac{d}{dt}f(\mathbf{X}, \mu, v_{\parallel}, t) = \left[\frac{\partial}{\partial t} + \dot{\mathbf{X}} \cdot \nabla + \dot{v}_{\parallel} \frac{\partial}{\partial v_{\parallel}} \right] f = 0, \quad (1)$$

where

$$\dot{\mathbf{X}} = v_{\parallel} \mathbf{b} + \mathbf{v}_E + \mathbf{v}_d$$

and

$$\dot{v}_{\parallel} = -\frac{1}{m} \frac{\mathbf{B}^*}{B} \cdot (\mu \nabla B + Z \nabla \phi).$$

The $f(\mathbf{X}, \mu, v_{\parallel}, t)$ is the distribution function with \mathbf{X} the gyrocenter, μ the magnetic moment and v_{\parallel} the parallel velocity. \mathbf{B} is the equilibrium magnetic field, $\mathbf{B}^* = \mathbf{B} + \frac{B v_{\parallel}}{\Omega} \nabla \times \mathbf{b}$, $\mathbf{b} = \mathbf{B}/B$ and \mathbf{v}_E and \mathbf{v}_d are the $\mathbf{E} \times \mathbf{B}$ drift velocity and magnetic drift velocity, respectively. ϕ is the perturbed electrostatic potential, Z is the ion charge and m its mass. The perturbed potential is decomposed into zonal and non-zonal components $\phi = \langle \phi \rangle + \delta \phi$, where $\langle \phi \rangle$ is the flux-surface averaged zonal mode.

In this work, in order to reduce particle noise, we use the δf method [51] for the ion species. The ion gyrocenter distribution function $f = f_0 + \delta f$ is separated into an equilibrium

part f_0 and a perturbed part δf . Equation (1) may be written as $Lf = 0$ and the propagator L can be decomposed into equilibrium L_0 and perturbed δL parts. So

$$L_0 = \frac{\partial}{\partial t} + (v_{\parallel} \mathbf{b} + \mathbf{v}_d) \cdot \nabla - \frac{1}{m} \frac{\mathbf{B}^*}{B} \cdot (\mu \nabla B) \frac{\partial}{\partial v_{\parallel}} \quad (2)$$

and

$$\delta L = \mathbf{v}_E \cdot \nabla - \frac{1}{m} \frac{\mathbf{B}^*}{B} \cdot (Z \nabla \phi) \frac{\partial}{\partial v_{\parallel}}. \quad (3)$$

The equilibrium distribution function satisfies $L_0 f_0 = 0$ so f_0 is the neoclassical solution (however f_0 is approximated to a local Maxwellian in our simulations). This way the perturbed distribution function can be calculated as $(L_0 + \delta L) \delta f = -\delta L f_0$. We define the particle weight as $w = \delta f/f$, so

$$\frac{d}{dt}w = (1-w) \left[-\mathbf{v}_E \cdot \frac{\nabla f_0}{f_0} + \frac{Z}{m f_0} \frac{\mathbf{B}^*}{B} \cdot \nabla \phi \frac{\partial f_0}{\partial v_{\parallel}} \right]. \quad (4)$$

We use the electrostatic hybrid model [44] for the electron species. The electron drift kinetic equation can be written as $Lf_e = 0$ where the electron distribution function can be described as the sum

$$f_e = f_{0e} + \delta f_e^{(0)} + \delta h_e.$$

The equilibrium distribution satisfies $L_0 f_{0e} = 0$. The lowest order perturbed distribution is adiabatic response $\delta f_e^{(0)} = f_{0e} \frac{e \delta \phi^{(0)}}{T_e}$ and the higher order perturbed distribution is non-adiabatic response δh_e . The non-zonal potential $\delta \phi$ can also be expanded order by order $\delta \phi = \delta \phi^{(0)} + \delta \phi^{(1)}$. The gyrokinetic Poisson equation for the non-zonal component in the lowest order $\delta \phi^{(0)}$ becomes

$$\frac{(\tau + 1) e \delta \phi^{(0)}}{T_e} - \frac{\tau e \delta \tilde{\phi}^{(0)}}{T_e} = \frac{\delta \bar{n}_i - \langle \delta \bar{n}_i \rangle}{n_0}, \quad (5)$$

where $\tau = T_e/T_i$, n_0 is the equilibrium electron density, tilde represent double-gyroaveraging and $\delta \bar{n}_i = \int \delta f d^3 v$.

The non-adiabatic electron particle weight is defined as $w_e = \delta h_e/f_e$, which is governed by

$$\frac{dw_e}{dt} = \left(1 - \frac{\delta f_e^{(0)}}{f_{0e}} - w_e \right) \left[-\mathbf{v}_E \cdot \nabla \ln f_{0e}|_{v_{\perp}} - \frac{\partial}{\partial t} \left(\frac{e \delta \phi^{(0)}}{T_e} \right) - (\mathbf{v}_d + \delta \mathbf{v}_E) \cdot \nabla \left(\frac{e \phi}{T_e} \right) \right]. \quad (6)$$

The non-zonal potential with the first order correction becomes

$$e^{\delta \phi/T_e} = e^{\delta \phi^{(0)}/T_e} - \frac{\delta n_e - \langle \delta n_e \rangle}{n_0} \quad (7)$$

with $\delta n_e = \int \delta h_e d^3 v$. Equations (6) and (7) can be repeated to reach higher order in the expansion. After a converge test, we found that a second order expansion is sufficient for this work. Finally, the zonal component of the potential is calculated from

$$\frac{\tau e (\langle \phi \rangle - \tilde{\phi})}{T_e} = \frac{\langle \delta \bar{n}_i \rangle - \langle \delta n_e \rangle}{n_0}. \quad (8)$$

3. Collisionless damping of zonal flow in LHD

3.1. Zonal flow damping in LHD with adiabatic electrons

First, we analyze the zonal flow damping in the LHD, which is a heliotron with a helical pole number of $l = 2$. Its main helical field has the $m = 2$ poloidal and $n = 10$ toroidal number. The flux surface shapes also vary along the toroidal direction. The model equilibrium used in the present simulations corresponds to the outward-shifted configuration.

The LHD has a number of field periods $N_{fp} = 10$, i.e. all equilibrium quantities including magnetic field and metric tensors are symmetric under a 0.2π rotation in the toroidal direction. That periodicity allows us to simulate one-tenth of the torus to capture the dynamics of the zonal flows. Full torus simulations give similar results at a higher computational cost. To ensure the toroidal periodicity in a global field-aligned mesh, we shift the grid points in the poloidal direction by an angle $\Delta\theta = 2\pi/(qN_{fp})$ after a toroidal circuit when only one field period is simulated. The LHD equilibrium quantities are represented on the equilibrium mesh in GTC, where the radial, poloidal, and toroidal grid numbers are, respectively, 200, 799, and 27 over one field period (i.e. one-tenth of the torus).

The radial domain in the current simulations is restricted from $\psi = 0.13\psi_x$ to $\psi = 0.23\psi_x$ (where ψ_x is the poloidal flux at the last closed flux surface) and the diagnostics are done on the $\psi = 0.18\psi_x$ flux surface where the rotational transform is $\iota = 0.42$ and the local inverse aspect ratio is $\varepsilon = r/R_0 \approx 0.05$. All m poloidal and n toroidal harmonics of the equilibrium are included in the simulations unless it is explicitly stated. Based on convergence studies, we simulate 60 particles per cell in the turbulence mesh with 120 radial grid points, 270 poloidal grid points and 9 parallel grid points over one-tenth of the torus. Only $n = 0$ harmonic is retained in these simulations in sections 3.1–3.3. The toroidal coupling with $n \neq 0$ harmonics is analyzed in section 3.4.

Figure 1 shows the time evolution of flux-surface average electrostatic potential $\langle\phi\rangle$ (normalized by its initial value) after an initial zonal gyrocenter density perturbation is imposed in GTC simulations with adiabatic electrons for different $k_r\rho_i$ values where ρ_i is the ion gyroradius. The zonal potential oscillates with a GAM frequency, which is damped by collisionless magnetic pumping effects on a fast time scale in the order of ion transit time. The zonal flow residue then reaches a quasi-steady state level, which could be further damped on a much longer time scale by toroidal or poloidal viscosity.

In figure 2 we show the frequency spectrum of the zonal potential from Fourier transform of the time history data shown in figure 1. The vertical red dashed line in figure 2 indicates the theoretical GAM frequency [15]. The zonal flow with a long wavelength ($k_r\rho_i = 0.07$) exhibits two distinct frequencies: a larger and wider peak of the GAM frequency at $\omega \approx 2.5c_s/R_0$, and a smaller and narrower peak with a lower frequency $\omega \approx 0.3c_s/R_0$. The LFO has been predicted by analytic theory and observed in earlier simulations by the EUTERPE and GENE codes [17]. GAM is observed in all

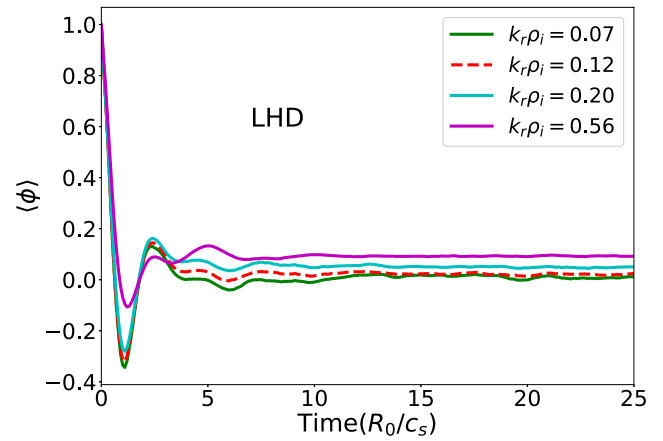


Figure 1. Time history of zonal potential in LHD for various radial wavenumbers $k_r\rho_i$.

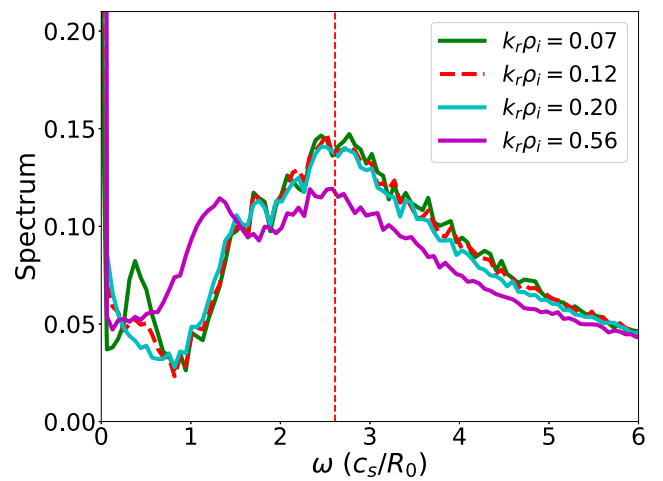


Figure 2. Time frequency spectrum of zonal flows shown in figure 1. Vertical red dashed line indicates theoretical GAM frequency.

cases but LFO is only visible for long wavelength modes ($k_r\rho_i \leq 0.12$).

3.2. Effects of kinetic electrons

To study kinetic electron effects on the collisionless damping of zonal flows, we perform a series of GTC simulations with kinetic electrons. Figure 3 shows a comparison between a simulation with adiabatic electrons (red dashed line) and kinetic electrons (green solid line) for a long wavelength $k_r\rho_i = 0.08$. The time evolution of the zonal potential shows a quite similar behavior. The frequency spectrum of the zonal potential (inset plot in figure 3) shows that the GAM frequency is the same but the LFO increases from $\sim 0.3c_s/R_0$ to $\sim 0.45c_s/R_0$ by the kinetic electrons. Furthermore, the kinetic electrons enhance the damping of the GAM and LFO.

Kinetic electrons also affect the quasi-steady state residual level of the zonal electrostatic potential. In figure 4 we plot the residual level from simulations with adiabatic or kinetic electrons for various $k_r\rho_i$ values. The analytical expression by Wang–Hahm [13] for the residual level for the axisymmetric

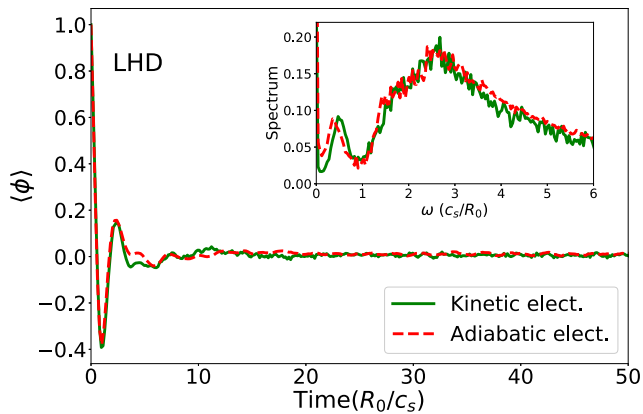


Figure 3. Time history of zonal electrostatic potential with initial $k_r \rho_i = 0.08$ for simulations with adiabatic electrons (red dashed line) and kinetic electrons (solid green line). Inset plot: frequency spectrum of zonal potential.

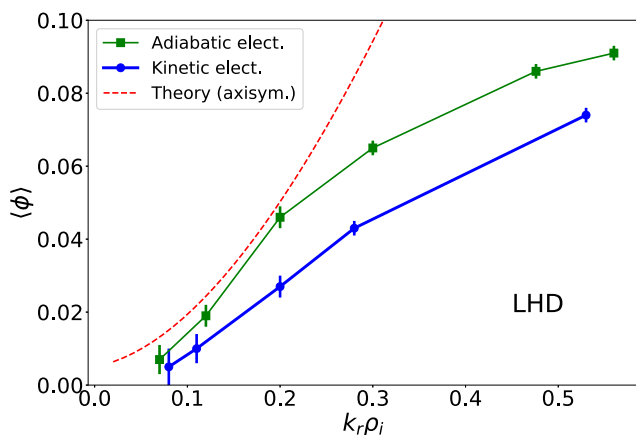


Figure 4. Residual level of zonal potential as a function of radial wavenumber $k_r \rho_i$.

tokamak is also plotted as a reference. The simulated residual levels are obtained by a temporal average over a time long enough ($\Delta t = 30R_0/c_s$) once the GAM oscillation amplitude diminishes. The error bars correspond to one standard deviation of that temporal average. The results show that the residual level increases as $k_r \rho_i$ increases [15, 17, 20]. Finally, simulations with kinetic electrons show that electron kinetic effects significantly reduce the residual level [21].

3.3. Effects of the helical components of the 3D magnetic field

The zonal flows in the stellarators exhibit, not only the GAM frequency (as in the tokamaks), but also a characteristic LFO, which has been predicted theoretically [17] to be induced by helically trapped particles. In the LHD model equilibrium used in this work, the main helical magnetic field is the $B_{(m=2,n=10)}$ component which is comparable to the $B_{1,0}$ component responsible for the GAM oscillation in both tokamaks and stellarators.

To verify that the main helical magnetic field component causes the LFO, we perform several controlled simulations with adiabatic electrons by selectively including various 3D

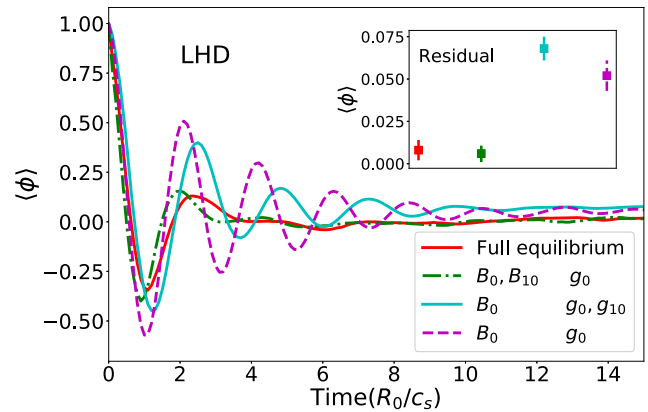


Figure 5. Time history of zonal potential from simulations with various magnetic field and metric tensor components. Subscript of B and g represents the toroidal harmonic n . Inset figure indicates residual levels for all simulations.

equilibrium effects. The equilibrium magnetic field and metric tensor can be represented as a summation of the toroidal harmonic n . Therefore, the equilibrium in GTC simulations can include some or all of the n harmonics for either the magnetic field or the metric tensor. Because of the stellarator symmetry of the LHD ($N_{fp} = 10$), we focus on the effect of the dominant $n = 10$ harmonics, which are responsible for the helically-trapped particles.

We perform four simulations by selectively including various helical components besides the axisymmetric ($n = 0$) component of the equilibrium: (a) the full 3D equilibrium including all toroidal harmonics n , (b) only the $n = 10$ harmonics in the magnetic field, (c) only the $n = 10$ harmonic in the metric tensor g , and (d) no 3D effects, i.e. only the axisymmetric ($n = 0$) harmonic in both magnetic field and metric tensor. Note that the equilibria (b) and (c) may not be self-consistent because the Jacobian depends on magnetic field strength in the Boozer coordinates. All m poloidal harmonics of the perturbed electrostatic potential were kept in the simulation. Figure 5 shows that including the $n = 0$ and 10 harmonics in the B field but only the $n = 0$ harmonic of the metric tensor recovers a similar result as the full equilibrium simulation. The frequency spectrum (not shown here) shows that the LFO is only visible if the $n = 10$ magnetic field B_{10} is included in the simulation. On the other hand, the GAM frequency is clearly visible in all the four simulations. This means that the main helical component B_{10} of the magnetic field generates the LFO, but not the GAM which is induced by the $n = 0$ axisymmetric component B_0 . Furthermore, both the B_{10} and the g_{10} components enhance the damping of the GAM oscillation, as predicted by analytic theory [15]. Finally, the main helical component B_{10} of the magnetic field reduces the residual level as shown in the inset panel of figure 5. The residual levels for the axisymmetric magnetic field (c) and (d) show a value above the Rosenbluth–Hinton residual level which is roughly ~ 0.02 . Such high value could be caused by the equilibrium shape [11].

3.4. Effects of linear toroidal coupling

In our previous simulations [9], a linear toroidal coupling of zonal flows with $n > 0$ harmonics was suggested to explain

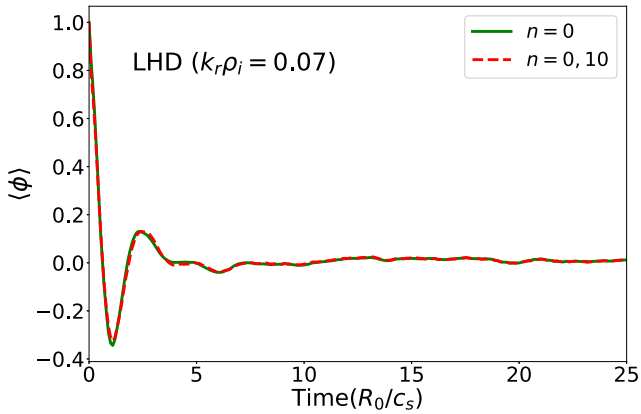


Figure 6. Time history of zonal electrostatic potential from simulations keeping only zonal mode (green solid line) or both zonal mode and $n = 10$ toroidal harmonic (red dashed line).

the effects of the zonal flows on the nonlinear spectrum of the ITG turbulence. The effect is caused by the toroidal variation of the magnetic field in the stellarators, which is dominated by the $n = 10$ harmonic in the LHD. Here, we carry out linear simulations with adiabatic electrons of the zonal flow damping in the LHD to analyze that mechanism.

Figure 6 shows the time history of the zonal electrostatic potential from two simulations of an initial zonal mode with a radial wavenumber $k_r \rho_i = 0.07$. The electrostatic potential has been filtered to allow only the $n = 0$ harmonic or both the $n = 0$ and $n = 10$ harmonics. The zonal mode (dominated by the $n = 0$ harmonic) can linearly couple to the $n = 10$ harmonic of the perturbed electrostatic potential due to the dominant helical component ($n = 10$) of the equilibrium magnetic field in the LHD. The simulation results show that linear toroidal coupling of the zonal mode to the $n > 0$ harmonics has little effects on the collisionless damping of the long wavelength zonal flow.

However, the zonal mode can generate low- n harmonics by the linear toroidal coupling. Figure 7 shows the time evolution of the amplitudes of various non-zonal components of the electrostatic potential normalized by the initial zonal mode amplitude. Besides the flux-surface averaged zonal mode, the axisymmetric component $\phi_{m=1,n=0}$ is the largest component followed by the second harmonic $\phi_{2,0}$. The largest non-axisymmetric components, $n = 10$, are much smaller than the axisymmetric $n = 0$ components. These results are compared with the components of the equilibrium magnetic field that induces these linear couplings. In the flux-surface of interest, the main harmonics of the magnetic field strength are

$$B_{0,0} > B_{1,0} > B_{2,10} > B_{1,10} > B_{3,10} > B_{2,0}.$$

The largest harmonic after the $B_{0,0}$ is the $B_{1,0}$. Similarly, the electrostatic potential $\phi_{1,0}$ is also the largest harmonic after the zonal mode $\phi_{0,0}$. This characteristic is also typical in axisymmetric tokamaks where there is a strong coupling between $\phi_{0,0}$ and $\phi_{1,0}$ due to the $B_{1,0}$. Similarly, the $\phi_{2,0}$ is generated mostly due to the $B_{2,0}$ component.

The helical components with $n \neq 0$, for example, $\phi_{2,10}$ and $\phi_{1,10}$, of the electrostatic potential are also generated due to the $n = 10$ harmonics of the magnetic field ($B_{2,10}, B_{1,10}$). However,

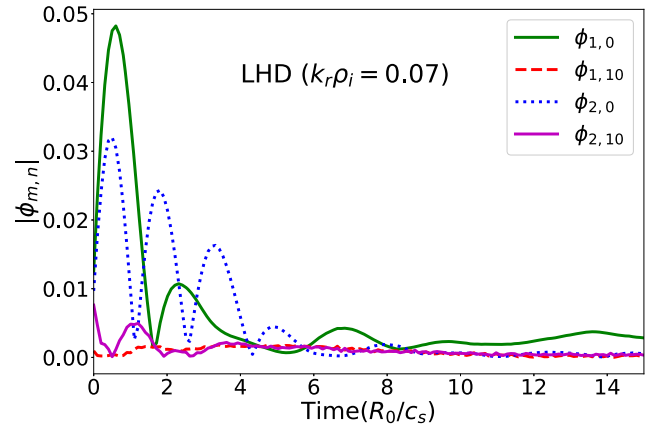


Figure 7. Time history of various non-zonal components of perturbed electrostatic potential ϕ .

the ordering of the magnitudes for these potential harmonics does not exactly match the ordering of the magnitudes for the magnetic field harmonics. The toroidal coupling seems to be relatively weaker than the poloidal coupling. In spite of the fact that the amplitudes of these $\phi_{2,10}$ and $\phi_{1,10}$ helical harmonics are much smaller than the axisymmetric harmonics $\phi_{1,0}$ and $\phi_{2,0}$, the low- n harmonics can act as quasi-modes to enhance the inverse cascade of the toroidal spectrum from the high- n unstable harmonics to the low- n damped harmonics [9].

4. Collisionless damping of zonal flows in W7-X

4.1. Zonal flow damping in W7-X with adiabatic electrons

A similar analysis of the collisionless damping of zonal flow is performed now for the W7-X stellarator. The magnetic field in the W7-X exhibits a strong variation along the toroidal direction peaking at the inner corners of the pentagon. In each field period the poloidal cross section shape considerably changes so the magnetic axis shows a helical structure. The rotational transform has little variation along the radial direction, i.e. the magnetic shear is weak. In this work, we use the high mirror magnetic configuration equilibrium which leads to a higher fraction of trapped particles than other configurations.

The W7-X has $N_{tp} = 5$ field periods so equilibrium quantities are symmetric after a 0.4π rotation in the toroidal direction. In a similar way as we did in section 3, the dynamics of zonal flows can be simulated using one-fifth of the torus taking advantage of that symmetry. The equilibrium quantities are represented on the equilibrium mesh, where the radial, poloidal, and toroidal grid numbers are, respectively, 200, 799, and 27 over one field period (i.e. one-fifth of the torus).

Radial simulation domain is restricted from $\psi = 0.44\psi_x$ to $\psi = 0.54\psi_x$ and the diagnostics presented here are done on the $\psi = 0.50\psi_x$ flux surface where the rotational transform is $\iota = 0.90$ and the inverse aspect ratio is $\varepsilon \approx 0.06$. Based on convergence studies, we simulate 80 particles per cell in the turbulence mesh with 120 radial grid points, 300 poloidal grid points and 9 grid points in the parallel direction. Only the $n = 0$ harmonic is retained in the simulations in

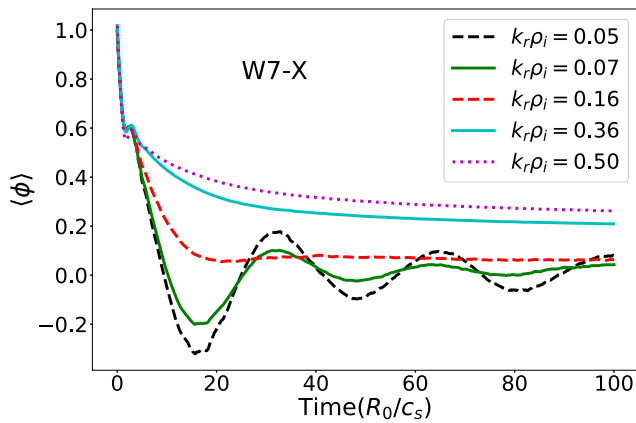


Figure 8. Time history of zonal electrostatic potential (normalized to its initial value) in W7-X from GTC simulations for various radial wavenumbers $k_r \rho_i$.

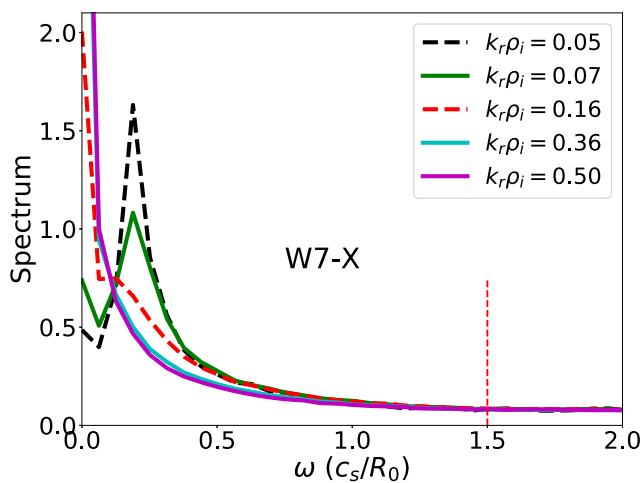


Figure 9. Frequency spectrum of zonal potential shown in figure 8. Vertical dashed line indicates GAM frequency.

sections 4.1–4.3. The toroidal coupling with $n \neq 0$ harmonics is analyzed in section 4.4.

Figure 8 shows the results from GTC simulations of the collisionless damping of the zonal electrostatic potential in the W7-X with adiabatic electrons for different values of initial wavenumber k_r . An oscillatory response is clearly observed for low values of k_r , but for values $k_r \rho_i > 0.15$ such oscillations are mostly damped. Frequency spectrum of these oscillations is shown in figure 9. The LFO frequency around $0.18c_s/R_0$ is very prominent for low values of k_r but not visible for $k_r \rho_i \gtrsim 0.15$. The GAM oscillation is not visible due to the strong Landau damping for the low safety factor $q = 1/\iota \sim 1.1$ [15, 17]. This large GAM damping was also observed in EUTERPE simulations of the TJ-II and W7-X stellarators [17, 22]. LFO frequency obtained by GTC ($\sim 0.18c_s/R_0$) agrees reasonably with the value $\sim 0.15c_s/R_0$ obtained by Monreal *et al* (see figure 12 in reference [29]) using CAS3D-K and EUTERPE.

4.2. Effects of kinetic electrons

To study the kinetic electron effects on the zonal flow damping, a set of GTC simulations of with kinetic electrons are

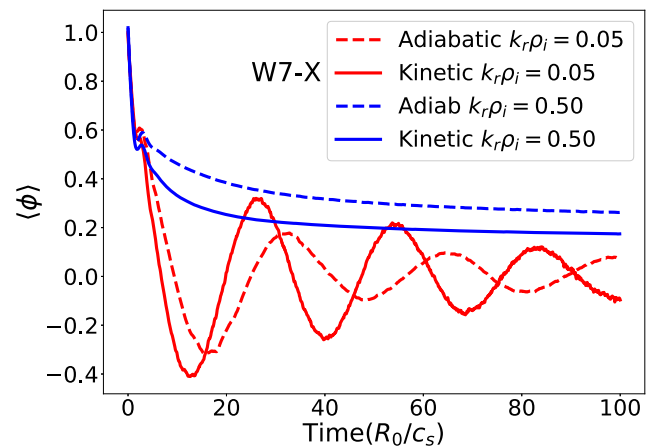


Figure 10. Time history of zonal potential (normalized to its initial value) in W7-X from GTC simulations with adiabatic electrons (dashed lines) and kinetic electrons (solid lines) for different values of $k_r \rho_i$.

carried out. Figure 10 shows the time history of the normalized flux-surface averaged electrostatic potential for a short (blue) and long (red) wavelengths with adiabatic (dashed lines) and kinetic (solid lines) electrons. For long wavelength zonal modes, the LFO is observed in both simulations but the electron kinetic effects increase the frequency from $\sim 0.18c_s/R_0$ to $\sim 0.25c_s/R_0$. For shorter wavelength zonal modes, the LFO is completely damped but the residual level of the simulation with kinetic electrons is lower.

The slow damping of the LFO in the W7-X for long wavelength zonal modes requires a much longer simulation time to determine its residual level, which is a *quasi-steady* state due to the weaker toroidal viscosity on a longer time scale. To obtain the residual level, we fit the zonal mode amplitude to the following time-dependent function

$$c_0 + c_1 e^{-c_2 t} \cos(c_3 t + c_4),$$

where c_0 is the residual value. Figure 11 shows the residual level from simulations with adiabatic and kinetic electrons for different values of $k_r \rho_i$. As a reference, a dashed line illustrates the analytical expression by Wang–Hahm [13] assuming an axisymmetric device with the inverse aspect ratio of $|B_{0,5}|/|B_{0,0}|$. We use the ratio of $|B_{0,5}|/|B_{0,0}|$ as the effective inverse aspect ratio in figure 11 because it determines the variations of the magnetic field. In tokamaks, the ratio of $|B_{1,0}|/|B_{0,0}|$ corresponds to the aspect ratio. Similar to the LHD, the residual value increases for shorter radial wavelength zonal mode. Kinetic electrons significantly reduce the residual level. The residual values and scaling from GTC simulations agree qualitatively with previously results by Monreal *et al* (see figure 9 in reference [24]), which used a different W7-X configuration.

4.3. Effects of the helical components of the 3D magnetic field

To verify that the helically-trapped particles induce the LFO, we now analyze the effects of the three dimensional equilibrium on the collisionless damping of the zonal flow in the W7-X stellarator. The main components of the magnetic field

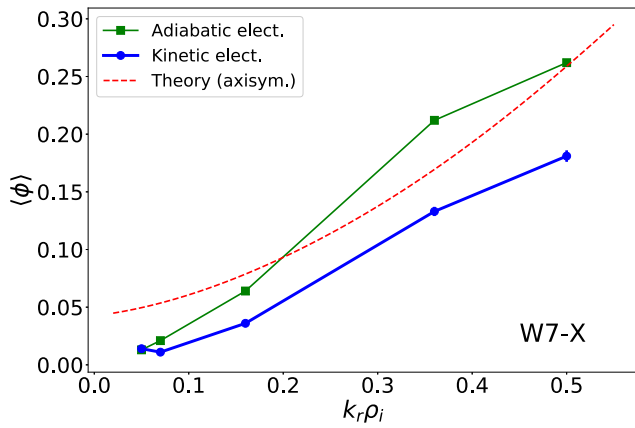


Figure 11. Zonal flow residual level as a function of radial wavenumber $k_r \rho_i$.

strength in the W7-X equilibrium used in this work are the $B_{0,5}$, $B_{1,5}$ and the (much weaker) axisymmetric $B_{1,0}$

$$B_{0,0} > B_{0,5} > B_{1,5} \gg B_{1,0}.$$

Several GTC simulations with adiabatic electrons are performed by including various 3D equilibrium effects besides the axisymmetric ($n = 0$) component. Four cases are simulated by incorporating various non-axisymmetric components: (a) the full equilibrium including all toroidal harmonics n (b) only the $n = 5$ harmonic of the B (c) only the $n = 5$ harmonic of the metric tensor g and (d) only the $n = 0$ axisymmetric equilibrium (i.e. no 3D effects). All m poloidal harmonics of the perturbed electrostatic potential were kept in the simulation. Figure 12 shows the time history of zonal potential (normalized to its initial value) using these four equilibria. The simulation results show that when the $n = 5$ harmonics of the magnetic field B_5 is included, the LFO can be observed. These harmonics include the $B_{0,5}$ and $B_{1,5}$, which are the main non-axisymmetric components. On the other hand, in the simulation with only the axisymmetric equilibrium (in the magnetic field and metric tensor) there is no LFO or GAM oscillations. The effect of the $n = 5$ harmonics in the metric tensor is not important for the LFO and GAM and only modifies the residual level of the zonal flow. Note that the GAM is always strongly damped in W7-X due to the rotational transform being close to unity. The residual level appears to be larger in the simulations without the $n = 5$ components in the magnetic field (the Rosenbluth–Hinton theoretical value is approximately 0.14) probably due to the shaping effect [11]. In further simulations with kinetic electrons, without the main helical component in the equilibrium, the electrons are no longer helically-trapped and their response is negligible as in the tokamak case. Hence, the axisymmetric case (d) in figure 12 shows same response with either adiabatic or kinetic electrons.

4.4. Effects of linear toroidal coupling

Figure 13 shows the time history of two different simulations with adiabatic electrons with the same initial zonal mode in the W7-X for a low $k_r \rho_i$. The electrostatic potential has been filtered to allow only the $n = 0$ harmonic or both the $n = 0$

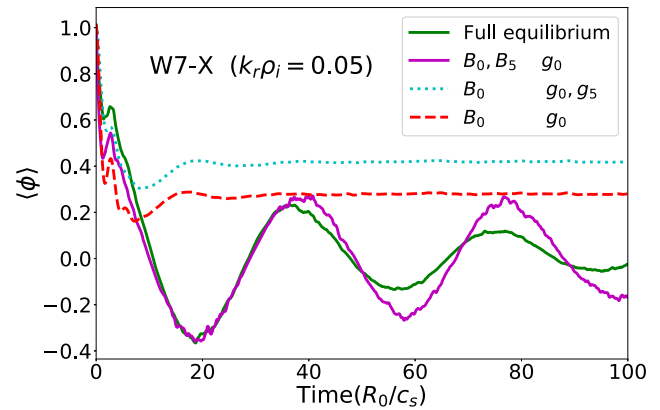


Figure 12. Time history of zonal potentials from GTC simulations incorporating various non-axisymmetric components of magnetic field and metric tensor in W7-X.

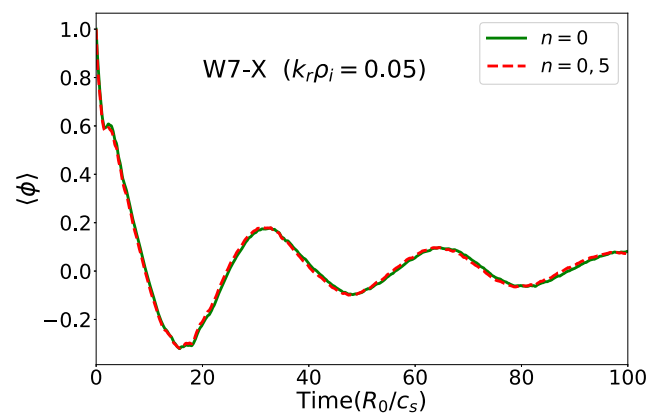


Figure 13. Time history of zonal electrostatic potentials (normalized by their initial values) in the W7-X from simulations filtering out all n harmonics except for the $n = 0$ (green solid line) or the $n = 0$ and $n = 5$ (red dashed line) harmonics.

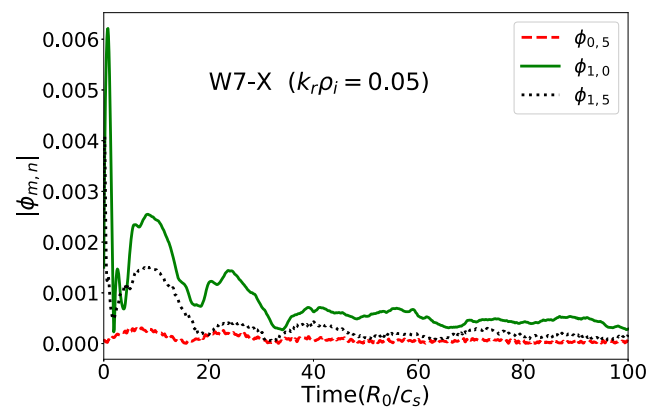


Figure 14. Time evolution of different non-zonal components of electrostatic potentials $\phi_{m,n}$ (normalized by the initial value of the zonal potential) from W7-X simulations.

and $n = 5$ harmonics. Due to the dominant non-axisymmetric $n = 5$ harmonics in the magnetic field of the W7-X, the $n = 0$ zonal mode can linearly couple with the $n = 5$ components of the electrostatic potential. The simulation results show little

effect of the linear toroidal coupling of the zonal mode to the non-zonal harmonic on the zonal flow dynamics.

On the other hand, the linear toroidal coupling has a significant impact on the generation of low- n harmonics. Figure 14 shows the time evolution of various non-zonal components normalized to the initial zonal potential. The axisymmetric component $\phi_{1,0}$ is the most dominant non-zonal component generated by the coupling despite the fact that the $B_{1,0}$ component is much smaller than the non-axisymmetric $B_{0,5}$ and $B_{1,5}$ components. The non-axisymmetric $\phi_{0,5}$ and $\phi_{1,5}$, generated due to the $n = 5$ harmonics of the magnetic field, are significantly smaller than the axisymmetric $n = 0$ component. Note that these low- n harmonics can enhance the inverse cascade of the toroidal spectrum from high to low n harmonics in turbulence simulations [9].

5. Conclusions

Global GTC simulations with kinetic electrons of collisionless damping of zonal flows in the LHD and W7-X stellarators have been carried out. The kinetic electrons reduce the zonal flow residue [24] and increase the frequency of the LFO. Simulation results show that the main non-axisymmetric harmonics of the magnetic field strength ($n = 10$ in the LHD and $n = 5$ in the W7-X) induce the LFO. The LFO is strongly damped, and becomes invisible, for large zonal flow wavenumbers, e.g. $k_r \rho_i \gtrsim 0.12$ in the LHD and $k_r \rho_i \gtrsim 0.15$ in the W7-X.

Furthermore, the linear toroidal coupling of multiple toroidal n -harmonics has been analyzed. Zonal flows appear to be not affected by coupling with $n > 0$ non-zonal components. On the other hand, a coupling between zonal flows and the non-zonal $n \neq 0$ components of the magnetic field generates low- n harmonics in the electrostatic potential, which is a new physics absent in the tokamaks. These low- n harmonics can act as *quasi-modes*, which enhance the inverse cascade from high- n unstable harmonics to low- n harmonics [9].

In the future, we plan to perform global gyrokinetic simulations of collisional damping of zonal flows in the W7-X and LHD. The collisions could increase the zonal flow damping and lead to an increase in turbulent transport [42, 43].

Acknowledgments

The W7-X model equilibrium used in this work was originally generated by J. Geiger. The authors would like to thank to J. Riemann, R. Kleiber, D.A. Spong, and H.Y. Wang for providing the equilibrium data of the LHD and W7-X. We acknowledge technical support by the GTC team. This work was supported by the U.S. Department of Energy, under Award No. DE-SC0018270 (SciDAC ISEP Center), DE-FG02-07ER54916, DE-SC0020413 and used the resources of the Oak Ridge Leadership Computing Facility at the Oak Ridge National Laboratory (DOE Contract No. DE-AC05-00OR22725) and the National Energy

Research Scientific Computing Center (DOE Contract No. DE-AC02-05CH11231).

ORCID iDs

Javier H. Nicolau  <https://orcid.org/0000-0003-1470-1820>
 Gyungjin Choi  <https://orcid.org/0000-0003-0044-1650>
 Jingyuan Fu  <https://orcid.org/0000-0002-8225-4156>
 Xishuo Wei  <https://orcid.org/0000-0001-7486-0407>
 Zhihong Lin  <https://orcid.org/0000-0003-2007-8983>

References

- [1] Dinklage A. et al 2018 *Nat. Phys.* **14** 855–60
- [2] Murakami S., Wakasa A., Maaberg H., Beidler C.D., Yamada H. and Watanabe K.Y. (LHD Experimental Group) 2002 *Nucl. Fusion* **42** L19
- [3] Edlund E.M., Porkolab M., Huang Z., Grulke O., Böttger L.-G., von Sehren C. and von Stechow A. 2018 *Rev. Sci. Instrum.* **89** 10E105
- [4] Klinger T. et al 2019 *Nucl. Fusion* **59** 112004
- [5] Helander P. et al 2020 Understanding energy confinement in Wendelstein 7-X *Invited Talk, 62nd Annual Meeting of the APS Division of Plasma Physics (Remote 2020)* (9–13 November 2020) p 65 (<https://meetings.aps.org/Meeting/DPP20/Session/VI01.5>)
- [6] Lin Z., Hahn T.S., Lee W.W., Tang W.M. and White R.B. 1998 *Science* **281** 1835
- [7] Diamond P.H., Itoh S.-I., Itoh K. and Hahn T.S. 2005 *Plasma Phys. Control. Fusion* **47** R35
- [8] Schmitz L. et al 2017 *Nucl. Fusion* **57** 025003
- [9] Wang H.Y., Holod I., Lin Z., Bao J., Fu J.Y., Liu P.F., Nicolau J.H., Spong D. and Xiao Y. 2020 *Phys. Plasmas* **27** 082305
- [10] Rosenbluth M.N. and Hinton F.L. 1998 *Phys. Rev. Lett.* **80** 724
- [11] Xiao Y. and Catto P.J. 2006 *Phys. Plasmas* **13** 082307
- [12] Xiao Y. and Catto P.J. 2006 *Phys. Plasmas* **13** 102311
- [13] Wang L. and Hahn T.S. 2009 *Phys. Plasmas* **16** 062309
- [14] Sugama H. and Watanabe T.-H. 2005 *Phys. Rev. Lett.* **94** 115001
- [15] Sugama H. and Watanabe T.-H. 2006 *Phys. Plasmas* **13** 012501
- [16] Mishchenko A., Helander P. and Könies A. 2008 *Phys. Plasmas* **15** 072309
- [17] Helander P., Mishchenko A., Kleiber R. and Xanthopoulos P. 2011 *Plasma Phys. Control. Fusion* **53** 054006
- [18] Winsor N. et al 1968 *Phys. Fluids* **11** 2448
- [19] Alonso J.A. et al 2017 *Phys. Rev. Lett.* **118** 185002
- [20] Matsuoka S., Idomura Y. and Satake S. 2018 *Phys. Plasmas* **25** 022510
- [21] Toda S., Nunami M. and Sugama H. 2020 *J. Plasma Phys.* **86** 815860304
- [22] Sánchez E. et al 2013 *Plasma Phys. Control. Fusion* **55** 014015
- [23] Zhang H.S. and Lin Z. 2010 *Phys. Plasmas* **17** 072502
- [24] Monreal P., Calvo I., Sánchez E., Parra F.I., Bustos A., Könies A., Kleiber R. and Görler T. 2016 *Plasma Phys. Control. Fusion* **58** 045018
- [25] Satake S., Sugama H. and Watanabe T.-H. 2007 *Nucl. Fusion* **47** 1258
- [26] Kleiber R., Hatzky R. and Mishchenko A. 2010 *Contrib. Plasma Phys.* **50** 766
- [27] Mishchenko A. and Kleiber R. 2012 *Phys. Plasmas* **19** 072316
- [28] Sánchez E., Calvo I., Velasco J.L., Medina F., Alonso A., Monreal P. and Kleiber R. 2018 *Plasma Phys. Control. Fusion* **60** 094003

- [29] Monreal P., Sánchez E., Calvo I., Bustos A., Parra F.I., Mishchenko A., Könies A. and Kleiber R. 2017 *Plasma Phys. Control. Fusion* **59** 065005
- [30] Smoniewski J., Sánchez E., Calvo I., Pueschel M.J. and Talmadge J.N. 2021 *Phys. Plasmas* **28** 042503
- [31] Sanchez E. *et al* 2021 Gyrokinetic simulations in stellarators using different computational domains *Nucl. Fusion* **61**
- [32] Beer M.A., Cowley S.C. and Hammett G.W. 1995 *Phys. Plasmas* **2** 2687
- [33] Connor J.W., Hastie R.J. and Taylor J.B. 1978 *Phys. Rev. Lett.* **40** 6
- [34] Sánchez E., Mishchenko A., García-Regaña J.M., Kleiber R., Bottino A. and Villard L. 2020 *J. Plasma Phys.* **86** 855860501
- [35] Cole M.D.J., Hager R., Moritaka T., Dominski J., Kleiber R., Ku S., Lazerson S., Riemann J. and Chang C.S. 2019 *Phys. Plasmas* **26** 082501
- [36] Navarro A.B. *et al* 2020 *Plasma Phys. Control. Fusion* **62** 105005
- [37] Spong D.A., Holod I., Todo Y. and Osakabe M. 2017 *Nucl. Fusion* **57** 086018
- [38] Fu J.Y., Nicolau J.H., Liu P.F., Wei X.S., Xiao Y. and Lin Z. 2021 *Phys. Plasmas* **28** 062309
- [39] Holod I., Lin Z., Taimourzadeh S., Nazikian R., Spong D. and Wingen A. 2017 *Nucl. Fusion* **57** 016005
- [40] Dong G. and Lin Z. 2017 *Nucl. Fusion* **57** 036009
- [41] Fang K., Bao J. and Lin Z. 2019 *Plasma Sci. Technol.* **21** 115102
- [42] Lin Z., Hahm T.S., Lee W.W., Tang W.M. and Diamond P.H. 1999 *Phys. Rev. Lett.* **83** 3645
- [43] Lin Z. *et al* 2000 *Phys. Plasmas* **7** 1857
- [44] Lin Z., Nishimura Y., Xiao Y., Holod I., Zhang W.L. and Chen L. 2007 *Plasma Phys. Control. Fusion* **49** B163
- [45] Xiao Y., Holod I., Wang Z., Lin Z. and Zhang T. 2015 *Phys. Plasmas* **22** 022516
- [46] Lin Z. *et al* 2002 *Phys. Rev. Lett.* **88** 195004
- [47] Riemann J., Kleiber R. and Borchardt M. 2016 *Plasma Phys. Control. Fusion* **58** 074001
- [48] Hirshman S.P. and Whitson J.C. 1983 *Phys. Fluids* **26** 3553
- [49] Lee W.W. 1983 *Phys. Fluids* **26** 556
- [50] Brizard A.J. and Hahm T.S. 2007 *Rev. Mod. Phys.* **79** 421
- [51] Parker S.E. and Lee W.W. 1993 *Phys. Fluids B* **5** 77